Deterministic earthquake scenario for the Basel area: Simulating strong motions and site effects for Basel, Switzerland

Ivo Opršal,[1] Donat Fäh, P. Martin Mai, and Domenico Giardini
Swiss Seismological Service, ETH-Zurich, Zurich, Switzerland

Received 24 May 2004; revised 1 November 2004; accepted 14 December 2004; published 19 April 2005.

[1] The Basel earthquake of 18 October 1356 is considered one of the most serious earthquakes in Europe in recent centuries (I_0 = IX, $M \approx 6.5–6.9$). In this paper we present ground motion simulations for earthquake scenarios for the city of Basel and its vicinity. The numerical modeling combines the finite extent pseudodynamic and kinematic source models with complex local structure in a two-step hybrid three-dimensional (3-D) finite difference (FD) method. The synthetic seismograms are accurate in the frequency band 0–2.2 Hz. The 3-D FD is a linear explicit displacement formulation using an irregular rectangular grid including topography. The finite extent rupture model is adjacent to the free surface because the fault has been recognized through trenching on the Reinach fault. We test two source models reminiscent of past earthquakes (the 1999 Athens and the 1989 Loma Prieta earthquake) to represent $M_w \approx 5.9$ and $M_w \approx 6.5$ events that occur approximately to the south of Basel. To compare the effect of the same wave field arriving at the site from other directions, we considered the same sources placed east and west of the city. The local structural model is determined from the area's recently established *P* and *S* wave velocity structure and includes topography. The selected earthquake scenarios show strong ground motion amplification with respect to a bedrock site, which is in contrast to previous 2-D simulations for the same area. In particular, we found that the edge effects from the 3-D structural model depend strongly on the position of the earthquake source within the modeling domain.

Citation: Opršal, I., D. Fäh, P. M. Mai, and D. Giardini (2005), Deterministic earthquake scenario for the Basel area: Simulating strong motions and site effects for Basel, Switzerland, *J. Geophys. Res.*, *110*, B04305, doi:10.1029/2004JB003188.

1. Introduction

[2] Reliable earthquake hazard assessment requires good regional coverage of strong motion observations as well as detailed microzonation studies for urban planning. The lack of observed strong ground motion data (due to no strong earthquakes) can be effectively remedied by numerical modeling in which source, path, and site effects are taken into consideration. Evaluating these predicted earthquake ground motions helps to understand better the associated seismic hazard and potentially allows to reduce the seismic risk by appropriate antiseismic design. The considered source models are calibrated via the solution of the inverse problem at particular site (Athens, Loma Prieta). The rupture is then modeled using the crustal structure for Basel with M_w conserved.

[3] Near-source ground motion simulation requires knowledge of the source processes, path, and site effects, as well as appropriate methods for numerical calculations. In this paper we use a hybrid technique which combines a physically realistic characteristics of the earthquake source, wave propagation toward the site of interest, and the FD method to evaluate combined local effects.

[4] The Basel event, considered the strongest historical earthquake in Central Europe, occurred in today's seismically moderate Rhine Graben area and reached intensity IX [*Fäh et al.*, 2001]. Its magnitude [*Meghraoui et al.*, 2001] is estimated to be M = 6.5. Recent interpretation of the historical observations reaches M = 6.9 [*Fäh et al.*, 2003]. The known historical evidence shows that local effects might have been very strong due to the soil structure in the Basel area. Moreover, trenching has shown that the potential earthquake source is located nearby about 10 km from the city [*Meghraoui et al.*, 2001]. The tremendous damage may be result of site effects in conjunction with strong near-source seismic radiation.

[5] Some recent events with strong near-field effects were the 1995 Hyogo-ken Nanbu earthquake (Japan) [*Irikura et al.*, 1999], the 1999 Athens (Greece), and 2002 Chi-Chi (Taiwan) earthquakes. Site effects, however, may also be very strong from a distant source, as observed for the 1989 Mexico or the 1884 Andalusian (Spain) [*Luzón et al.*, 2004]

[1] On leave from Faculty of Mathematics and Physics, Department of Geophysics, Charles University, Prague, Czech Republic.

0148-0227/05/2004JB003188$09.00

earthquakes. The so-called "edge effect" is another dangerous ground motion phenomenon. It is connected to the basin structure and results in pronounced damage belts of relatively narrow compact regions and large structural damage as observed for instance, in the 1995 Hyogo-ken Nanbu event [*Irikura et al.*, 1999]. Synthetic strong motion scenarios may help us to better understand and predict the unknown phenomena in deterministic hazard assessment.

[6] In our work we use realistic earthquake scenarios, modeled as finite extent ruptures that follow composite and pseudodynamic approaches. The seismic waves excited by these sources are then propagated through the local structure of the Basel city, calculated with a hybrid three-dimensional (3-D) FD method that combines all source path site effects.

2. Structure Details of the Basel Area: Upper Rhine Graben, Digital Model

[7] Numerical modeling of the 3-D site effects requires detailed knowledge of the 3-D subsurface structure, and site geology. The highest level of the geotechnical investigations consists of a 3-D model of the physical parameters (seismic velocities, densities, thickness, damping) and their respective uncertainties. Previous work for the Basel area has delivered detailed maps of the soil structure (thickness and composition, water table depth, and geotechnical information [*Kind*, 2002; *Fäh et al.*, 1997; *Noack et al.*, 1999; *Noack*, 1993; F. Kind et al., Seismic zonation from a 3D seismic velocity reference model of the area of Basel, Switzerland, submitted to *Bulletin of the Seismological Society of America*, 2003, hereinafter referred to as Kind et al., submitted manuscript, 2003]), while in situ measurements of the soil properties were performed to constrain the seismic velocities, and soil–bedrock interface. Since shear wave propagation velocity is the most important material property for site effects, various methods were applied to determine these velocities, including seismic reflection measurements, surface wave techniques, and analysis of seismic ambient vibrations [*Fäh et al.*, 1997; *Kind*, 2002; *Kind et al.*, 2005; Kind et al., submitted manuscript, 2003]. All available data were collected to construct a structural 3-D model for the city of Basel and its vicinity [*Kind*, 2002; Kind et al., submitted manuscript, 2003]. That model serves as input for our 3-D FD modeling of combined site effects.

[8] Although real geological structures might be very complex, computational methods often require averaged or smoothed material properties in the computational model. The reasons for such smoothing may be numerical (e.g., averaging parameters in FD grid) or a fundamental restriction of the method (ray tracing in the smooth media). Thus the chain "geological structure" → "digital geological model" → "computational model" must be realized [see *Opršal and Zahradník*, 2002]. The digital model is then available as a function $\mathbf{a} = \mathbf{a}(\mathbf{X})$, where $\mathbf{a}$ is a parameter vector ($\mathbf{a} = (\lambda, \mu, \rho, Q_p, Q_s, \ldots)$) for each position vector $\mathbf{X} = (x, y, z)$. The meaning of the symbols is as follows: λ, μ are Lamé's material parameters; ρ is density; Q_p, Q_s denote the quality factors for P and S waves, respectively; and x, y, z are the spatial coordinates.

[9] The 3-D digital model for the Basel area (20 km × 18 km) comprises of six main interfaces and the topography. Each of the six layers between the main interfaces consist of mutually parallel sublayers that always follow the overlying surface topography. The 3-D geologic structure of the Basel area has been compiled and integrated into a digital model [*Zechner et al.*, 2001; *Kind*, 2002]. The interface geometry between the first four geologic units of the model (QUA, TUE, ALS, MEL; see Figure 1) is based on the distinct lithology at the bottom of the Quaternary sediments, as mapped from the database of boreholes in the Basel area [*Noack*, 1993]. The geophysical parameters for the region were compiled by *Fäh et al.* [1997] and *Steimen et al.* [2003]. The S wave velocities were recently specified by application of an array technique to ambient vibrations measured on five array sets in Basel [*Kind*, 2002]. Estimated error in that S wave velocity model is about 10–15%. A deep borehole provided caliber, gamma ray/density and sonic logs (GPI Basel, unpublished data, 2001). For the refinement and verification of the model geometry, *Kind* [2002] and Kind et al. (submitted manuscript, 2003) used H/V polarization analysis to estimate the fundamental frequencies at 250 measurement sites within the Rhine Graben (160 of them were located within or close to the Basel city). A conservative error estimate of the fundamental frequency measurements yields uncertainty of about 15%. Measured versus calculated fundamental frequencies from the initial 3-D model led to the correction of the geometry of the interfaces. The geophysical parameters at depths of more than 100 m are not well determined.

[10] Typical S wave velocity values close to the free surface are $v_s \approx 450–650$ m s^{-1} reaching $v_s = 800–1200$ m s^{-1} at 500 m depth, while the P wave velocity is about constant ($v_p \approx 1800$ m s^{-1}) for layers QUA, TUE, ALS, and MEL (Figure 1). The deeper layers (UPM, MES, PCB ≡ infinite bedrock) have following S wave velocities: $v_p \approx 3400–5200$ m s^{-1} and $v_s \approx 2000–2800$ m s^{-1} (identical with the properties of the last three layers defined in Table 1).

[11] To compute amplification effects with respect to a bedrock site, we use the reference bedrock model (Table 1) by *Fäh et al.* [1997], successfully used by *Kind* [2002] and *Kind et al.* [2005, submitted manuscript, 2003]. The source is the same for the 3-D model and the reference bedrock structure, and they both include topography. The topography of the area and the location of the city with respect to the Rhine Graben master fault are depicted in Figure 2.

3. Three-Dimensional Hybrid Method

[12] Modern numerical modeling approaches of near-source ground motions are directed toward three-dimensional methods to include complex source path site effects. We computed these effects in the area of Basel with the two-step hybrid technique of *Opršal and Zahradník* [2002]. In the first step, the FD, ray, discrete wave number (DWN) method or, in principle, any 3-D ground motion method (sometimes even an analytical solution is applicable) is used to compute particle motion at the surfaces of an imbedded permeable excitation box that envelopes the local structure of interest. The source in our computations is a finite extent source (see below). Results from the first step are saved and then used as input using a wave injection algorithm in the second step [*Opršal et al.*, 2002]. The second step is a second-order 3-D FD method on irregular

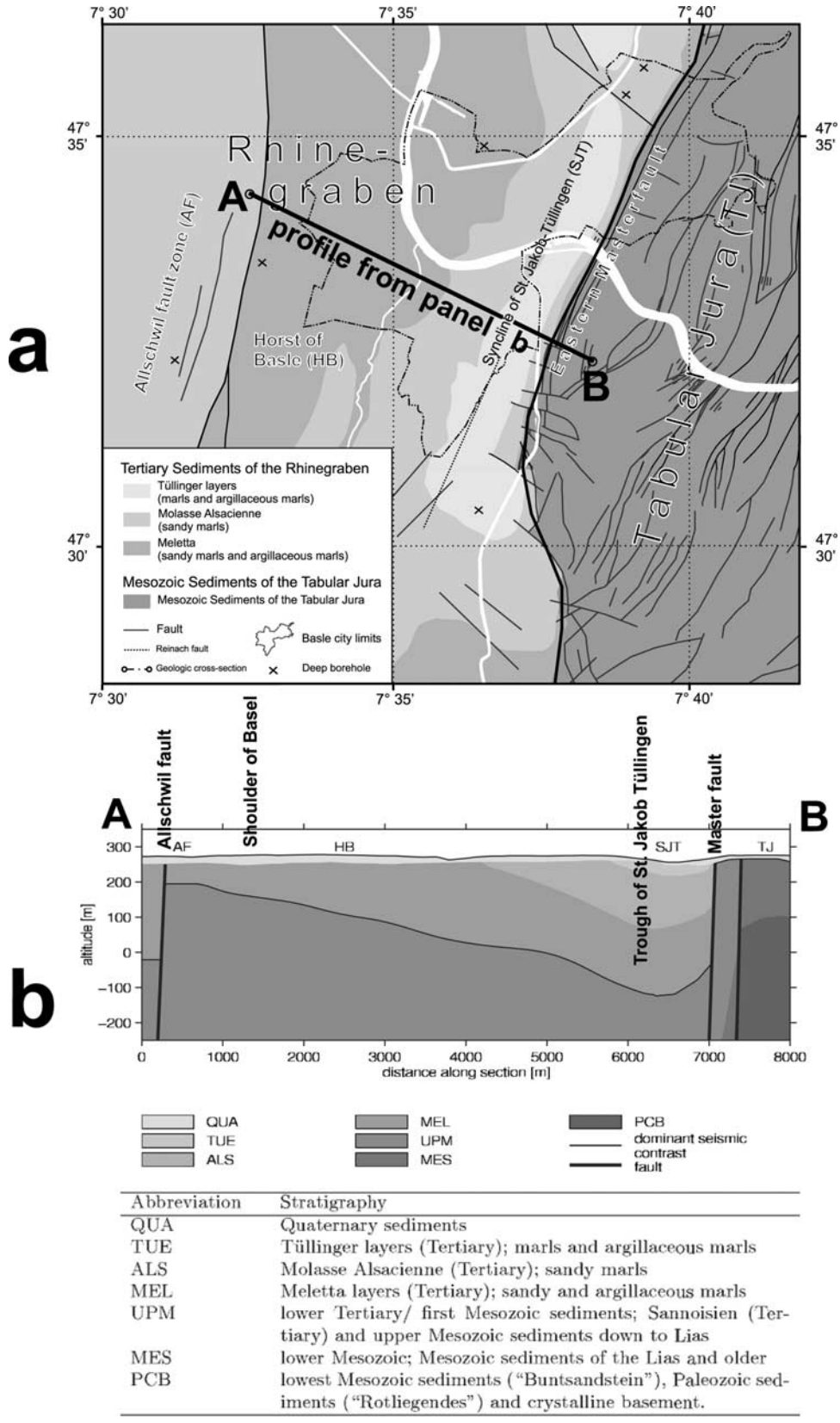

Abbreviation	Stratigraphy
QUA	Quaternary sediments
TUE	Tüllinger layers (Tertiary); marls and argillaceous marls
ALS	Molasse Alsacienne (Tertiary); sandy marls
MEL	Meletta layers (Tertiary); sandy and argillaceous marls
UPM	lower Tertiary/ first Mesozoic sediments; Sannoisien (Tertiary) and upper Mesozoic sediments down to Lias
MES	lower Mesozoic; Mesozoic sediments of the Lias and older
PCB	lowest Mesozoic sediments ("Buntsandstein"), Paleozoic sediments ("Rotliegendes") and crystalline basement.

Figure 1. (a) Stratigraphic units below the surface Quaternary sediments in the Basel area. (b) Representative E-W cross section of the geology in Basel. The dominant seismic *S* wave velocity contrast is indicated as a line between MEL and UPM. The table represents the stratigraphic units represented by the abbreviations (modified after *Kind* [2002]).

Table 1. One-Dimensional Vertical Profile Used as Reference Model[a]

Depth, km	ρ, g/cm^3	V_p, km/s	Q_p	V_s, km/s	Q_s
0.01	2.30	3.00	50	1.00	25
0.02	2.30	3.10	50	1.40	25
0.03	2.30	3.15	50	1.80	25
0.14	2.40	3.20	50	1.85	25
0.26	2.40	3.30	50	1.91	25
0.38	2.40	3.40	50	1.97	25
0.50	2.40	3.40	50	1.97	25
0.90	2.50	3.40	50	2.00	25
1.00	2.55	4.20	75	2.40	35
10.0	2.65	5.20	125	2.80	50

[a]Depth, ρ, V_p, Q_p, V_s, and Q_s are the depth of the top of next layer, density, *P* wave velocity, *P* wave quality factor, *S* wave velocity, and *S* wave quality factor, respectively.

grids with topography. This hybrid technique separates the source and regional path effects from the site effects, thus needing less computer resources than all-in-one methods (e.g., direct FD computation). A similar formulation in 3-D has been recently introduced by *Bielak et al.* [2003] and *Yoshimura et al.* [2003] in finite elements–finite elements (FE-FE) method.

[13] In our first step, source and path effects are computed for three different sources. The excitation box in our case extends from the free surface to a depth of ~3 km and encompasses the local site of interest. Complete particle motion histories for points on the surfaces of the excitation box are saved on disk [*Opršal and Zahradník*, 2002; *Opršal et al.*, 2002]. Propagation of the wave field from the source to the Basel site is realized by the DWN method. It is based on a 3-D analytical Green's function computation (summation in frequency *f* and wave number *k* domains) for 1-D layered linear viscoelastic media. The synthetic DWN seismograms containing the complete response of the earthquake source and the path effects (near, intermediate, and far field of the representation theorem) are then used in the second step to perform full 3-D FD computations of wave propagation through the local site structure.

3.1. First Step: Realistic Source Models

[14] One of our goals is to simulate the response to the historical M_w = 6.9 Basel earthquake of 1356 [*Fäh et al.*, 2003]. Although it was one of Europe's strongest events, its source mechanism is poorly known and the error in the magnitude estimate is ±0.5 units. A large level of uncertainty also contaminates the intensities inferred for the

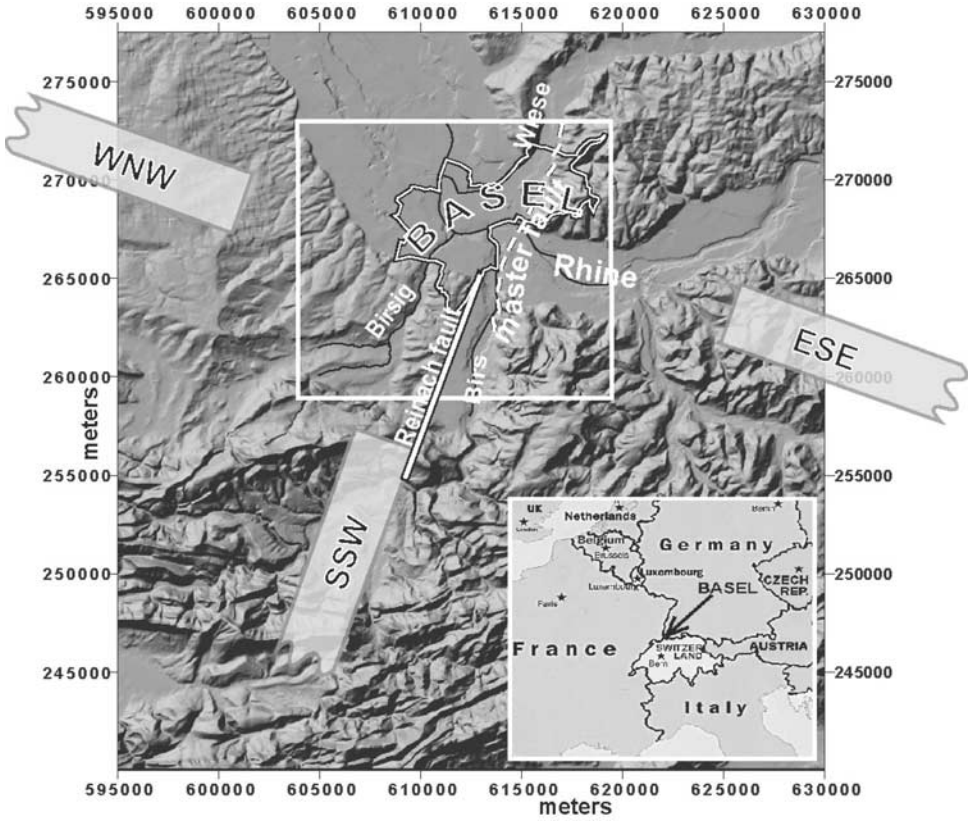

Figure 2. Top view of the area of interest, showing the topography of the computational model. The lines denote as follows: solid black and white, Basel city limits; dashed black and white, the surface trace of the Rhine Graben master fault; black, rivers Rhine, Wiese, Birs, and Birsig; and the solid black and white line, the surface trace of the Reinach fault. The white rectangle demarks the area shown in the further results and approximately coincides with the excitation box. The investigated positions of the finite extent source are given by WNW, SSW, and ESE partial projections of the rupture. The coordinates are in meters (the Swiss coordinate system). For secondary faults, see Figure 6. The relief panel is modified from digital height model DHM25, by SwissTopo, March 1999.

historical event that could provide rough estimates of the source characteristics.

[15] The northernmost point of the 1356 earthquake fault plane is considered to be located on the Rheinach fault starting at the city limits of Basel [*Meghraoui et al.*, 2001; *Kind*, 2002]. In our calculations we assume that the northernmost position of the rupture is located ~8 km south of Basel, outside the excitation box. Positioning the rupture closer to the city will be realized in future research. The Rheinach fault plane has a strike of 199°, and a dip of 75°. Depending on the source model realization, the rupture plane is either buried (M1) or extending to the free surface (M2, M3). The respective hypocenters are approximately 12 km and 10 km deep.

[16] Additionally, we computed ground motion with source locations east and west of the city of Basel to study the directional dependence of amplification effects. Such sources are not very likely for our study area since most of the faults have a strike similar to that of the Reinach fault. It is our intent, however, to examine the effects of the same *S* wave field arriving at the site of interest from other incidence angles to asses how the impeding waves interact with the fixed structure. The strike of the three source locations is 289°, 199°, 109°, respectively, corresponding approximately to WNW, SSW, and ESE positions with respect to the city. For SSW position of fault, the northernmost part of rupture is located 9 km south of the Basel city limits (Figure 2). As specified below, well-studied 1989 Loma Prieta and 1999 Athens events were selected as the scenario sources. The former was chosen because its magnitude is in the range of the approximate magnitude of the 1356 Basel event, the latter represents a smaller event that has a larger probability of occurrence. The source models (see below) conform with the tectonics in the area: The depth of the Moho discontinuity is ~20 km, and the events are distributed mainly around strike slip and around normal fault.

3.1.1. The 1999 Athens Earthquake (M1)

[17] Our first model is similar to the M_w = 5.9, 1999 Athens earthquake computed by the PEXT method [*Zahradník and Tselentis*, 2002]. This method models a finite extent source whose complexities are represented by stochastic perturbation and extrapolation (PEXT) of the low-frequency deterministic wave field. The low-frequency part contains the near, intermediate and far-field terms, as well as the effects of the free surface and 1-D structure. In contrast to the referenced paper (where perturbation was performed in high- and low-frequency part), all perturbations and extrapolations are applied here for the high-frequency part only since here the low-frequency part is treated as purely deterministic. The low-frequency part remains unchanged. Composite source modeling is realized by DWN [*Coutant*, 1989; *Bouchon*, 1981] calculation of the point source synthetics for a set of equally sized (and relatively few) subevents. Their moment rate is expressed by Brune's causal time function in the frequency domain):

$$(2\pi f_c)^2/(2\pi f_c + 2\pi i f)^2,$$

where f_c is corner frequency, $i^2 = -1$, and f is frequency. Each subevent is subject to empirical Green's function-like summation and low-frequency enhancement [*Irikura and Kamae*, 1994]. The deterministic calculations presented here go slightly beyond the corner frequency of the subevents, where the summation is incoherent. Hence the source possesses realistic directivity. After that, a shaping window is derived from these low-frequency acceleration time series. Finally, Gaussian noise, shaped by the time window (obtained before), is generated, having a flat acceleration spectrum (omega-squared model with f^{-2} falloff above the known corner frequency in displacement). This procedure defines the phase of the stochastic high-frequency radiation, where the amplitude is then same as that of the deterministic spectral plateau; the attenuation correction (kappa effect) is employed a posteriori.

[18] The fault length of the 1999 Athens event estimated from low-frequency seismic data is about 15 km; that from high-frequency information was considerably smaller. The latter was supported by early aftershocks as shown by *Oprsal et al.* [2004, Figure 3]. Therefore we consider a single asperity 4.0 km × 4.8 km, with slip contrast of 2.2 (consistent with *Somerville et al.* [1999]); the source composed of 5 × 5 = 25 subevents, each subevent with the slip duration is $1/f_c$ = 0.57 s, and average slip is 0.059 m. The nucleation point is assumed to be at the depth of 10 km at the bottom corner of the asperity. For the rest of the rupture area, a homogeneous slip is set to maintain the moment. The upper edge of the fault plane is at 8 km depth. Rupture propagates radially with velocity v_r = 2.8 km s^{-1} (≡ 80% of the local *S* wave velocity), with a 10% perturbation of the rupture time to improve the coherence in the high-frequency summation. The average slip velocity on asperity is (average slip) times (slip contrast)/(rise time) = 0.059 × 2.2/0.57 m s^{-1} = 0.23 m s^{-1}. The maximum slip velocity depends on the wavelet used, and, in the case of Brune's wavelet it is (average slip velocity × 2.3) = 0.52 m s^{-1}. The deterministic modeling is carried out up to 2.8 Hz, and the resulting acceleration spectral plateau (averaged between 2.0 and 2.8 Hz) is stochastically extrapolated up to 6 Hz.

[19] The source model was verified against the strong motion acceleration waveforms recorded in the central part of Athens (see Figure 3) [*Kalogeras and Stavrakakis*, 1999; *Ambraseys et al.*, 2000]. The dominant frequencies of velocities were about 0.6 Hz. For more details and comparison against the accelerograms, see *Serpetsidaki* [2004] and *Oprsal et al.* [2004].

3.1.2. The 1989 Loma Prieta-Like Models (M2, M3)

[20] For the next class of source models we chose a rupture characterization similar to the 1989 Loma Prieta earthquake, with the rupture plane penetrating the topmost sedimentary layers (in the 1-D reference model) up to the surface. The source dimensions of the rupture plane are chosen according to source-scaling relations [*Mai and Beroza*, 2000] and results from fault trenching, leading to a width and length of the rupture plane of 12 km × 27 km, respectively, with a dip angle of 75°. Since this source size is considerably smaller than the inferred rupture zone for the 1989 Loma Prieta earthquake (14 km × 40 km), we also reduced the seismic moment to M_w = 6.5 with respect to the original Loma Prieta model (M_w = 6.9), resulting in more realistic ground motion amplitudes.

[21] We allow surface rupture for these two scenario events, and hence the bottom part of the fault is at a depth

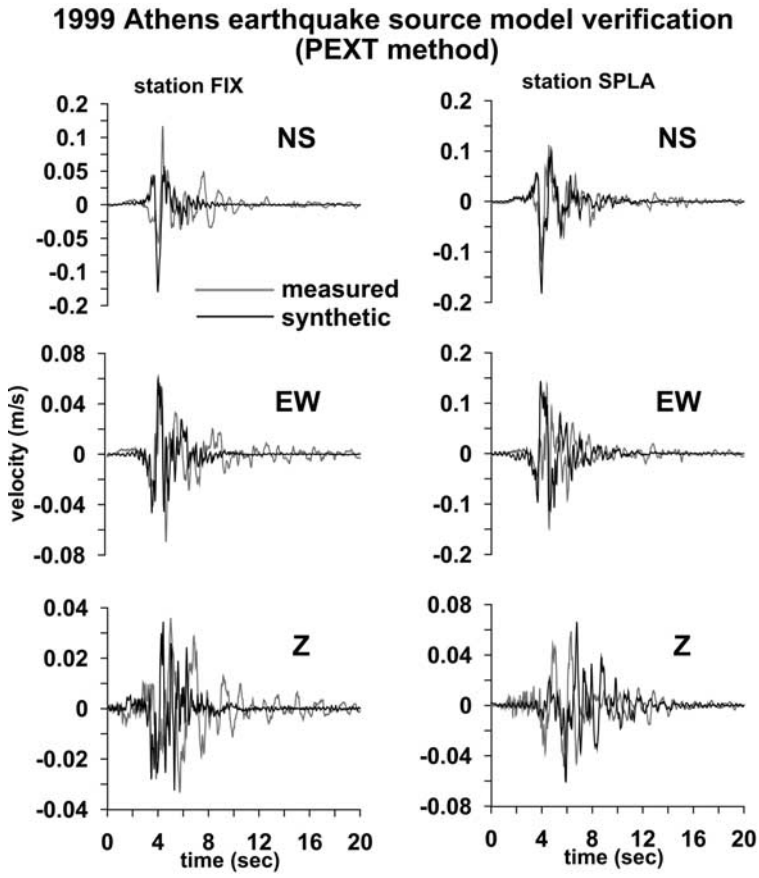

Figure 3. Comparison of the PEXT synthetic velocities with strong motion data verifying the source model for north-south, east-west, and vertical components, respectively. High-frequency oscillations in the synthetics are due to frequency window that is sharper than for the real seismogram. For more details, see *Zahradník and Tselentis* [2002] and *Opršal et al.* [2004].

of 11.5 km for the chosen W × L dimensions of the rupture zone, and the dip. The final slip distributions of such source models (Figure 4) are computed based on the spatial random field model for earthquake slip [*Mai and Beroza*, 2002].

[22] To generate a physically self-consistent rupture model, we deploy the pseudodynamic source characterization proposed first by *Mai et al.* [2001], and then further developed by *Guatteri et al.* [2003, 2004]. In purely kinematic source models, the rupture velocity and risetime are chosen without considering the underlying dynamics of earthquake rupture. In contrast, the pseudodynamic source model uses the static stress drop corresponding to the final slip distribution to approximate the fracture energy on the rupture plane. This distribution of fracture energy is then used to calculate physically consistent distributions of rupture velocity and risetime. The final source model therefore comprises realistic spatial and temporal variations in the slip, rupture propagation and risetime (Figure 4).

[23] Here, the hypocenter is a predefined parameter, but it strongly influences the rupture propagation and resulting risetime distribution. The two presented models M2 and M3 differ in the position of their hypocenters (Figure 4), allowing to discriminate the effects of directivity from source model rupturing "toward" (M2) and "away from" (M3) the site of interest. Ground motions were propagated to the site of interest (as an input for the FD) by DWN-FE method of *Olson et al.* [1984], using the COMPSYN code [*Spudich and Xu*, 2003]. We use the frequency domain Kostrov approximation as the local slip velocity source time function [*Mai et al.*, 2001]. An example of the resulting ground motion velocities due to source and directivity effects is shown in Figure 5.

3.2. Second Step: FD Method

[24] The linear elastic FD method [*Opršal and Zahradník*, 2002] is a second-order displacement approximation to the elastodynamic equation. It uses one FD template in the whole computational model on an irregular, rectangular grid, including free surface topography (vacuum formalism) that is approximated by a staircase-like boundary. Internal boundaries are approximated by averaged material parameters to satisfy internal boundary conditions [*Zahradník*, 1995; *Opršal and Zahradník*, 2002]. For bench marking of the method, see *Opršal and Zahradník* [2002] and *Opršal et al.* [2002]. Nonreflecting boundaries and supplement tapers are employed at the edges to simulate transparency. The FD formulation is stable for complex models with high v_p/v_s contrasts and high (v_p/v_s) ratio contrasts. In the following, the synthetic FD computations are accurate within the frequency band 0–2.2 Hz, where we consider

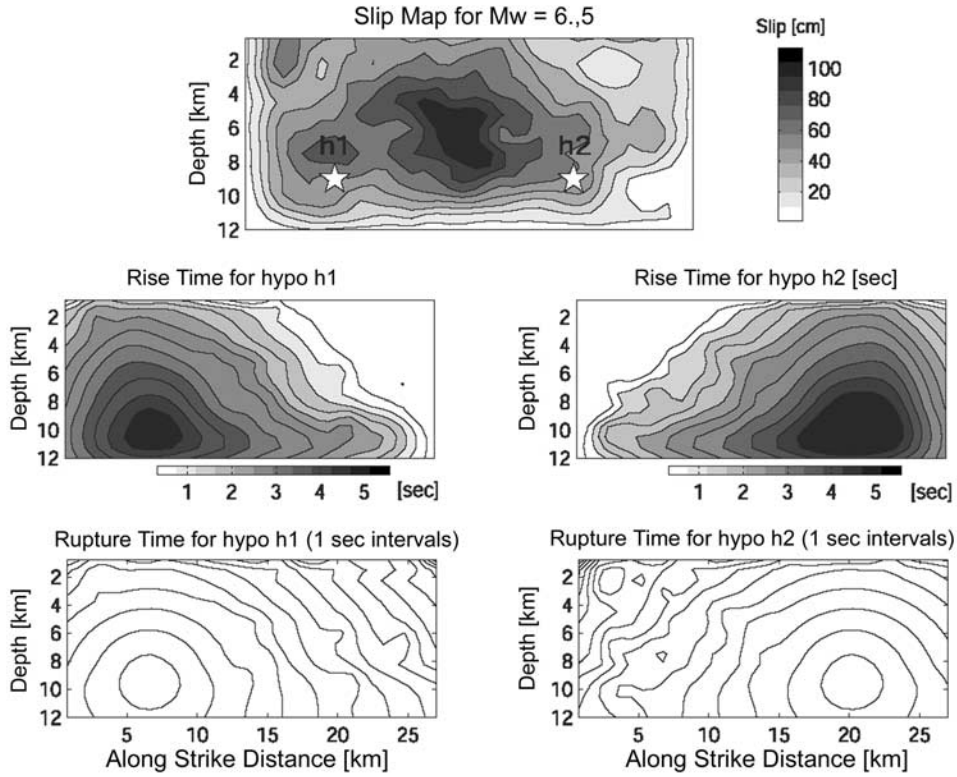

Figure 4. Final slip distribution used for M2 and M3 rupture histories, Loma Prieta-like earthquake (M_w = 6.5). Hypocenters, H1 and H2 stars, are corresponding to the M2 and M3 rupture histories, respectively. Both H1 and H2 are situated 3 km from the bottom part and 6 km from the corresponding sides of the rupture zone. The dimensions of the fault are 12 km × 27 km, downdip distance is measured from the intersection of the fault plane with flat free surface. Propagation of the rupture is "toward" (M2, H1) and "away from" (M3, H2) the Basel site (see also Figure 2).

at least 10 grid points per the shortest S wavelength everywhere in the model.

3.3. Attenuation

[25] The wave field propagating from the source to the local structure is computed in an perfectly elastic medium. Effects of intrinsic attenuation are introduced via an a posteriori correction in the frequency domain, controlling mainly high-frequency decay of the acceleration spectra by multiplication of an exponential term $e^{-\pi\kappa f}$ (f is frequency in Hz and κ is the attenuation parameter). Typical values of κ range from κ = 0.01 s for tectonically very stable regions up to κ = 0.06 s (e.g., for Greece κ = 0.05 s [*Margaris and Hatzidimitriou*, 2002]). Generally, κ varies locally due to site conditions, but to constrain its actual value is difficult. For Basel we used κ = 0.03 s, which corresponds to tectonically quieter region.

[26] In the FD part, the wave propagation in anelastic media is approximated by a single Q factor without distinguishing the P and S waves (for 2-D case, see *Zahradník et al.* [1990a, 1990b]):

$$Q(f_{\text{prev}}) = Q_p = Q_s = Q(x,y,z) = cf_{\text{prev}};$$

where f_{prev} is the prevailing frequency of the signal and corresponds to the frequency of maximum amplitudes of the signal spectrum. Conveniently, f_{prev} may be approximated in the center of the considered frequency interval. Choosing f_{prev} in such way allows for $Q(f_{\text{prev}}) = Q_s$ since the signal is considered quasi-monochromatic, where the S or surface wave field is usually of the highest interest. Factor a is added to the elastodynamic equation in the form of an absorption force:

$$\tau_{ij,j} + f_i = \rho u_{i,tt} + a\rho u_{i,t},$$

thus $a = 2\pi f_{\text{prev}}/Q(f_{\text{prev}})$; τ being the stress tensor, f_i is ith component of body force, u displacement, and t time; indices $,_k$ and $,_t$ mean partial derivative with respect to kth spatial component or time, respectively. In the 3-D case, this approach has been used for a 3-D staggered grid FD by *Graves* [1996]. The values used in our computations are as follows f_{prev} = 1 Hz, $Q(f_{\text{prev}})$ = 25 for depth <800 m, $Q(f_{\text{prev}})$ = 50 for depth >2000 m, and Q has a constant gradient for depth $\in \langle 800, 2000 \rangle$ m (corresponding to average vertical profile in the model).

3.4. Computational Details

[27] Computation of 30 s history of the excitation by the DWN method took about 10 hours for PEXT method and about 50 hours for the pseudodynamic modeling. By far, the most demanding was the FD part of the second step. An FD model with variable grid step from 27 m up to 156 m in all 3 directions occupied approximately 1.8GB of core memory. One second of the time history then needed about 5.5 hours

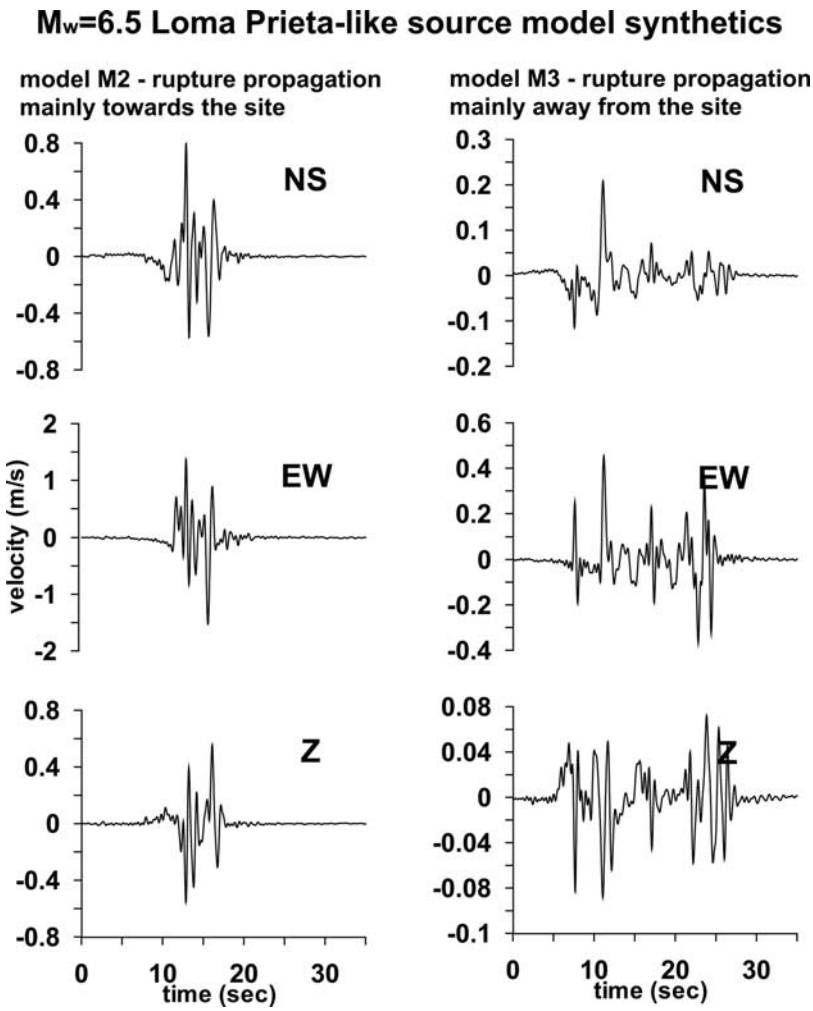

Figure 5. Example of the strong ground motion velocity synthetics for the M_w = 6.5 Loma Prieta-like earthquake. The receiver is placed on the free surface approximately in the direction of the fault at about 7 km north of the rupture. The two different rupture models (Figure 4) result in different length, amplitudes, and frequency content of the wave field.

of computer time; all on a Pentium 4, 2.6 GHz. The entire FD domain comprised about 5.1×10^7 grid points, and the time step was 0.0027 s. Total computed time history varied from 25 to 40 s, depending on the length of the excitation. Parallel runs of the code (using OMP) were performed on the IBM SP4 machines using three nodes for a shared memory mode with speedup above 2.5.

4. Parameters of Investigation

4.1. Response and Fourier Spectra

[28] In analyzing our results, we accommodated engineering needs by using pseudoacceleration response spectra (PSA) computed from synthetic signals for the receivers placed at the free surface. To represent the variability of and differences in damage potential within the studied area, we computed the spectral amplification. It is defined as the PSA ratio between the results obtained with the 3-D model and the reference (mainly 1-D) structure. Such a ratio quantifies the amplification effects at a specific site, and can be compared with results obtained by *Kind* [2002] from two-dimensional modeling with *SH* wave propagation. The 3-D results were compared to the 2-D ones but a detailed investigation, in terms of wave propagation, of similarities and discrepancies of the site responses is beyond the scope of this article. For all of the following we used the total horizontal PSA with 5% critical damping for 50 log-regularly distributed frequencies between 0.1 Hz and 2.5 Hz.

[29] High sensitivity of PSA to time shifts or the shape of considered signal is a good indicator for the motions of a building. As an addition, Fourier spectra (FS) of horizontal components of the ground motion velocity were evaluated for certain points to demonstrate filtering features in the local structure. The PSA is smoother and the peaks are broader than the absolute value of FS.

4.2. Fundamental Frequencies: Comparison With Synthetics

[30] Fundamental frequencies f_0 of resonance of soft sediments can be estimated from H/V spectral ratios of recorded ambient vibrations. This has been done by *Kind* [2002] for the Basel area (Figure 6, left). Multiple time windows in the measured signal have been used to compute an average H/V noise spectra ratio. In case of known

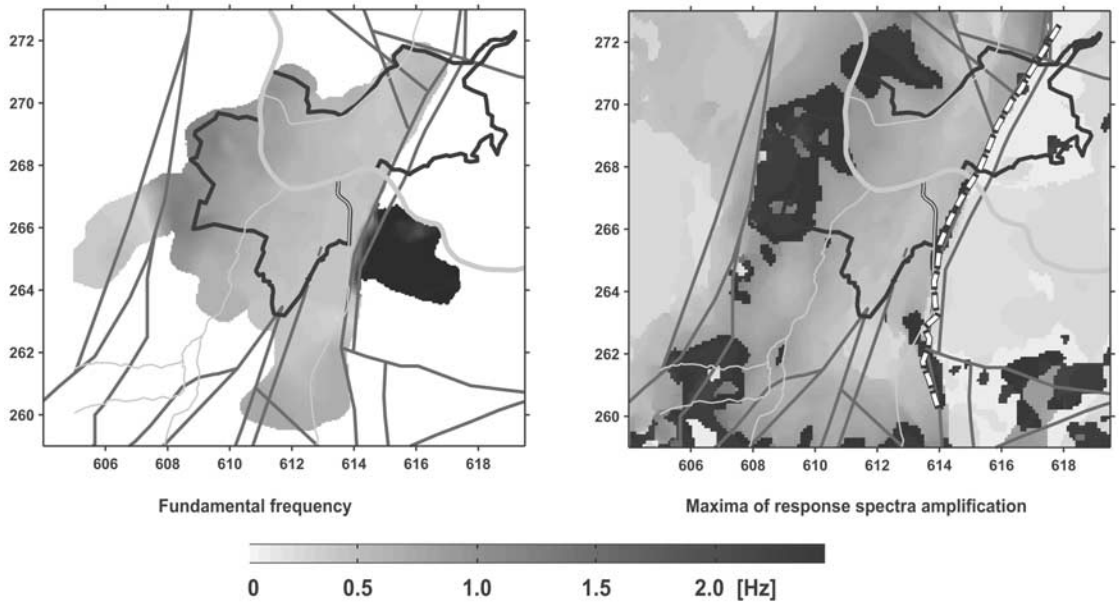

Figure 6. Comparison of (left) measured fundamental frequencies [*Kind*, 2002] and (right) frequencies corresponding to the computed maximum amplification of pseudoacceleration response spectra (coordinates in m). The lines denote as follows: thick black, Basel city limits; dashed black and white, the surface trace of the Rhine Graben master fault; gray, rivers; thick gray, the Rhine river; the remaining black lines, surface traces of faults. In Figure 6 (left), the regions of no data are white, while the black patch southeast of the city represents fundamental frequencies in 3–8 Hz range [*Kind*, 2002]. The coordinates are in km (the Swiss coordinate system).

thickness h of the soft sediments (e.g., from borehole information or seismic measurements), H/V spectral ratios can be used to estimate the average shear wave velocity v_s with the simple formula

$$v_s = 4 f_0 h.$$

[31] The effect due to the resonance at the fundamental frequency should be visible in synthetic ground motions. Generally, the frequencies with maximum PSA are not directly related to the fundamental resonance frequencies. In our narrow bandwidth case, however, the frequencies corresponding to the PSA amplification peaks coincide with the fundamental frequencies [see also *Kind*, 2002]. To apply excitation signals with as flat spectrum as possible, a vertically incident planar S wave pulse is used to excite the 3-D model. Figure 6 shows a comparison between the PSA amplification result for the vertically incident wave (Figure 6, right) and the fundamental frequencies measured for ambient noise (Figure 6, left). The agreement in spatial frequency distribution is very good. Because the synthetic signals are frequency band limited, we recognize a resonance effect only for frequencies below $f = 2.2$ Hz. The most affected parts of the city are patches in the southeast, outside the Rhine Graben (614 km east, 265 km north). The fundamental frequency and the frequency of the maximum PSA amplification follow the main geologic features given in cross section in the Figure 1. The Allschwil fault, situated 1–2 km west of the city limits, aligns very well with the border between higher and lower frequency of the maximum PSA amplification, even though the fault does not outcrop to the free surface. Similar phenomena are pronounced patches of higher frequency along the master fault. Such a sharp boundary is not present in the measured data, probably because of the interpolated results (from H/V measurements) and also because the synthetic data are evaluated only for vertical incidence. Because of a different approach in defining PSA and H/V maxima, the corresponding frequencies of the former are relatively higher than those of the latter, as it is apparent in the eastern part of the city.

5. Strong Ground Motions Due to Combined Source Path and Site Effects

[32] The results are compared for the three source models times three source positions as described in section 3.1.

Figure 7. Amplification zonation for particular zones covering the city of Basel and its vicinity, displayed for the three source models (M1, M2, M3) and then three different positions of the fault plane used in the 3-D modeling (see Figure 2). The spatial extent of five (fundamental) frequency zones [*Kind*, 2002] (see also Figure 8) with the frequency increasing from the southeast to the northwest are indicated by gray scale. For each zone a gray line shows the maximum amplification from all points inside this zone, while black lines correspond to the average amplification over all points determined for each event separately. Averaged/enveloped curves over all sources and source positions are in the bottom panels, where the thick black line denotes the envelopes of the averaged PSA amplifications (see also Figure 8).

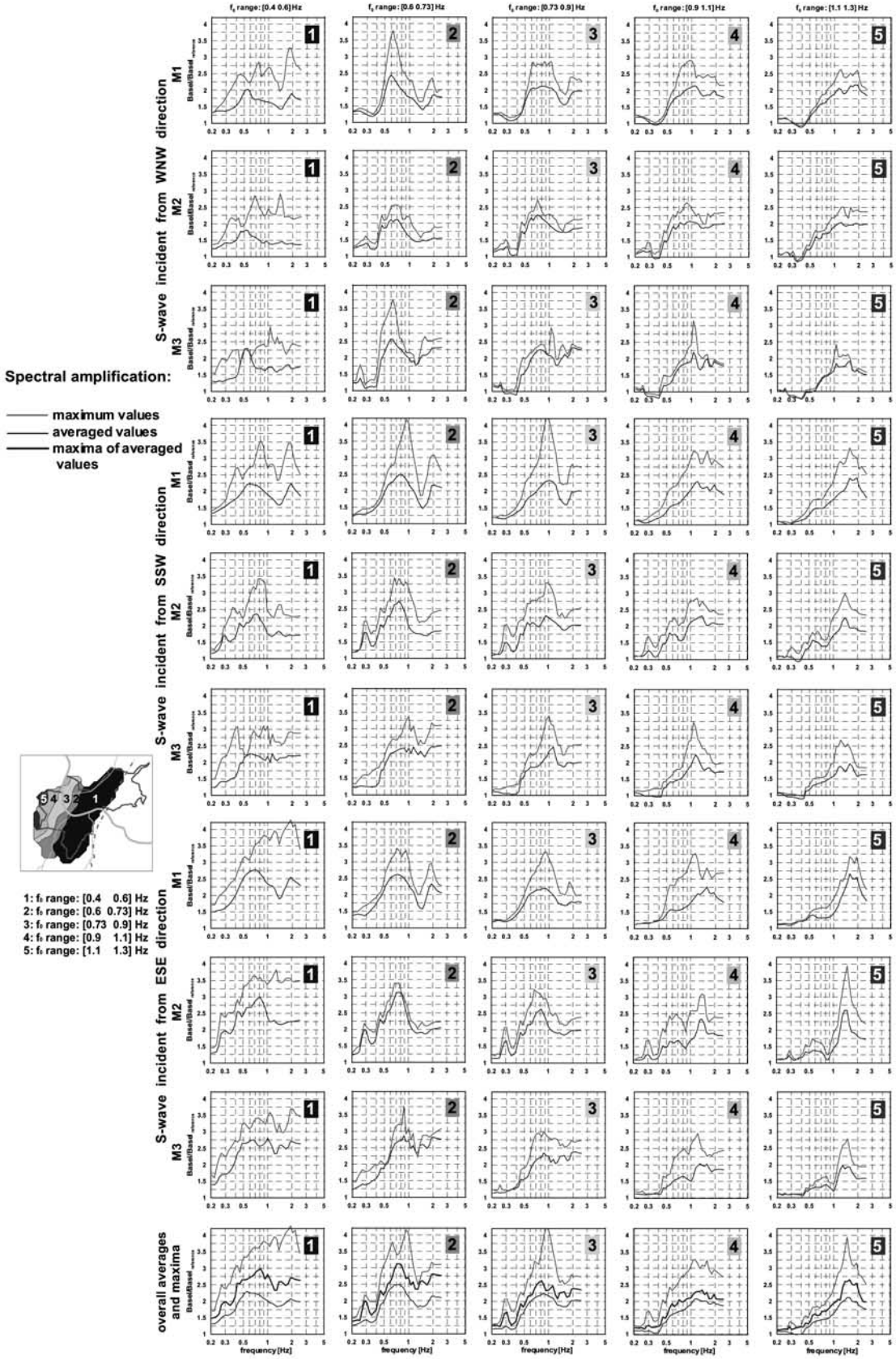
f0 range: [0.4 0.6] Hz
f0 range: [0.6 0.73] Hz
f0 range: [0.73 0.9] Hz
f0 range: [0.9 1.1] Hz
f0 range: [1.1 1.3] Hz
S-wave incident from WNW direction
S-wave incident from SSW direction
S-wave incident from ESE direction
overall averages and maxima
M1
M2
M3
Basel/Basel
frequency [Hz]
Spectral amplification:
maximum values
averaged values
maxima of averaged values
1: f0 range: [0.4 0.6] Hz
2: f0 range: [0.6 0.73] Hz
3: f0 range: [0.73 0.9] Hz
4: f0 range: [0.9 1.1] Hz
5: f0 range: [1.1 1.3] Hz

Figure 7

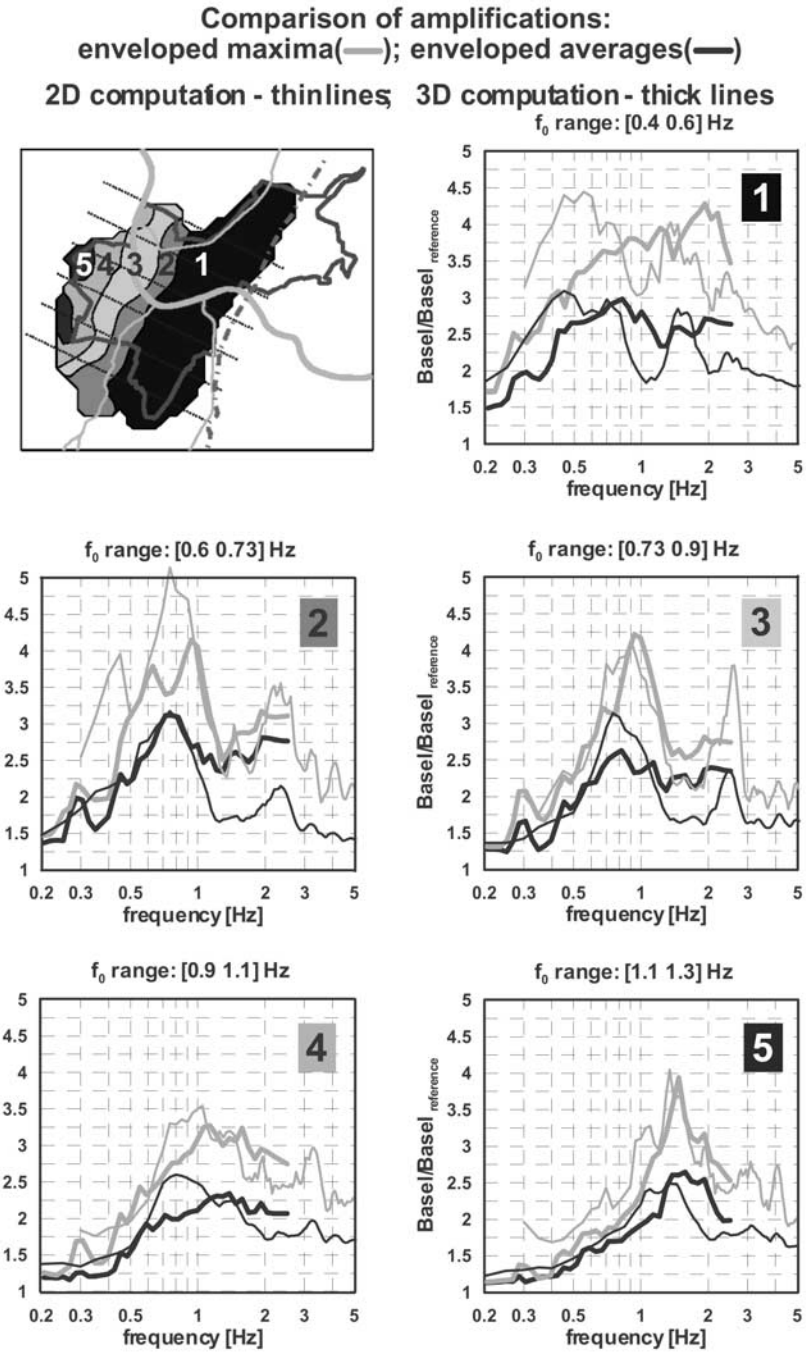

Figure 8. Comparison of the spectral acceleration amplification for particular zones covering the city of Basel. (top left) The spatial extent of the zones [*Kind*, 2002] with the fundamental frequency increasing from the southeast to the northwest (indicated by numbers). The thick lines 1–5 correspond to 3-D modeling results (Figure 7), the thin lines were obtained by 2-D *SH* modeling for various cross sections and 84 earthquake scenarios by *Kind* [2002]. For each zone, the gray lines show the overall maximum amplification from all 3-D scenarios; the black lines denote the envelope of the average amplification curves as depicted in Figure 7.

Direct comparison between M2 and M3 works because the earthquake is of the same magnitude and the only difference in models is the direction of rupture propagation. The directivity of the source plays a very important role in the frequency content and amplitudes of ground motion. Model M1 is for a smaller event; thus the frequency content is shifted toward higher frequencies.

5.1. Spectral Amplification Zonation (M1, M2, M3)

[33] The 2-D *SH* wave propagation effects around Basel were previously studied by *Kind* [2002] using a hybrid 2-D

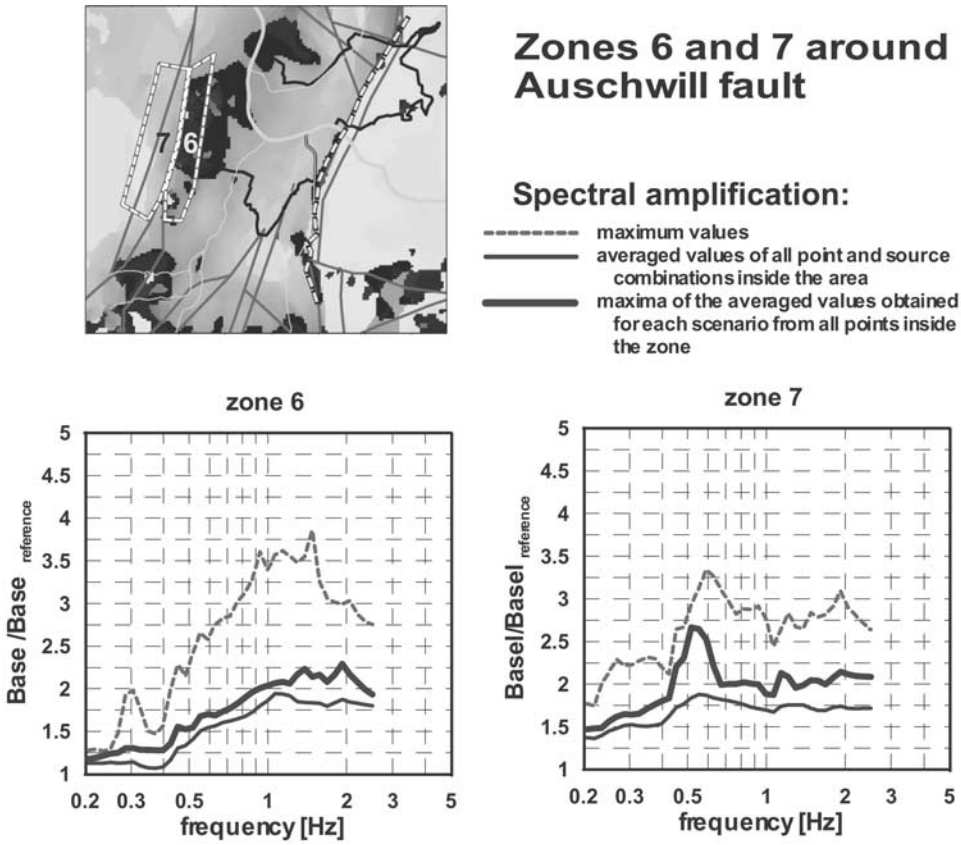

Figure 9. Two additional zones 6 and 7 (black and white dashed loops) around the Allschwil fault (see also Figure 1). (top left) Zones with respect to the city limits, showing the frequencies corresponding to the maxima of the PSA (as shown in Figure 6). The spectral amplifications for zones 6 and 7 and all scenario combinations of M1,M2,M3 source mechanisms and WNW, SSW, ESE source locations for each panel. We show the overall envelopes taken for each point and scenario, envelopes of averages for all points in a zone and each scenario, and average of all points in a zone and scenarios. The black and white dashed line is the surface trace of the Rhine Graben master fault.

methodology combining the modal summation and FD [*Fäh et al.*, 1994]. *Kind* [2002] performed a series of 2-D computations for various point source mechanisms, depths, distances and positions. FD computations were performed for 2-D and 1-D (reference is Tabular Jura) structural models. PSA was then computed for six individual sections of surface receivers (see below) for each source scenario. Basel city was subdivided into five zones by considering the ranges of the sediments' fundamental frequency of resonance. For more details, see *Kind* [2002, chapter 5]. Amplifications obtained for each zone were collected, and the result is shown below as a comparison to our 3-D case.

[34] The 3-D behavior, presented in this paper, was studied similarly as by *Kind* [2002]; the five spatial zones were unchanged. The computations were performed for all free surface receivers located in the 3-D model. A relatively high density of 100 surface receivers per km^2 assured approximately 200 points for analysis even for the smallest zone 5, defined by (1.1–1.3) Hz fundamental frequency. This analysis of 3-D simulations was performed independently for the three models (M1, M2, M3): each combined with three source positions (see Figure 7) corresponding to *S* waves arriving mainly from WNW, SSW, and ESE directions, respectively. The enveloped results from M1 models are systematically larger than those for M2 and M3. The best overall fit between the enveloped and averaged results is for the M2 models. The largest differences between the shape of the averaged and enveloped results are in zone 1. The largest spectral amplification ~4 to 4.25 is always reached for the M1 source for ESE (~2 Hz, zone 1) and SSW (~0.9 Hz, zone 2; ~1 Hz, zone 3) positions of rupture. As indicated in Figure 7, PSA amplification is very sensitive to source position and the arriving wave field, giving the variability factor of 1.75 for (both) the mean and maximum observed peak PSA amplifications throughout. The data for each zone were averaged and enveloped over all sources and source models. Figure 7 (left) also provides numbered denomination of the zones 1–5. Figure 8 compares averaged and enveloped M2, M3, M1-source simulations to the 2-D analysis results of *Kind* [2002]. In terms of PSA amplification, particular zones in the Basel area can be characterized as follows (see also Figure 7, left):

[35] 1. Zone 1 is at (0.4–0.6) Hz, with 2397 receivers: Pronounced amplification for (0.4–0.7) Hz band (enveloped averages) into two peaks at 0.8 Hz and ~2 Hz is similar as observed in the 2-D modeling, but the 0.8 Hz peak is shifted from 0.45 Hz in two dimensions. The pronounced peak at

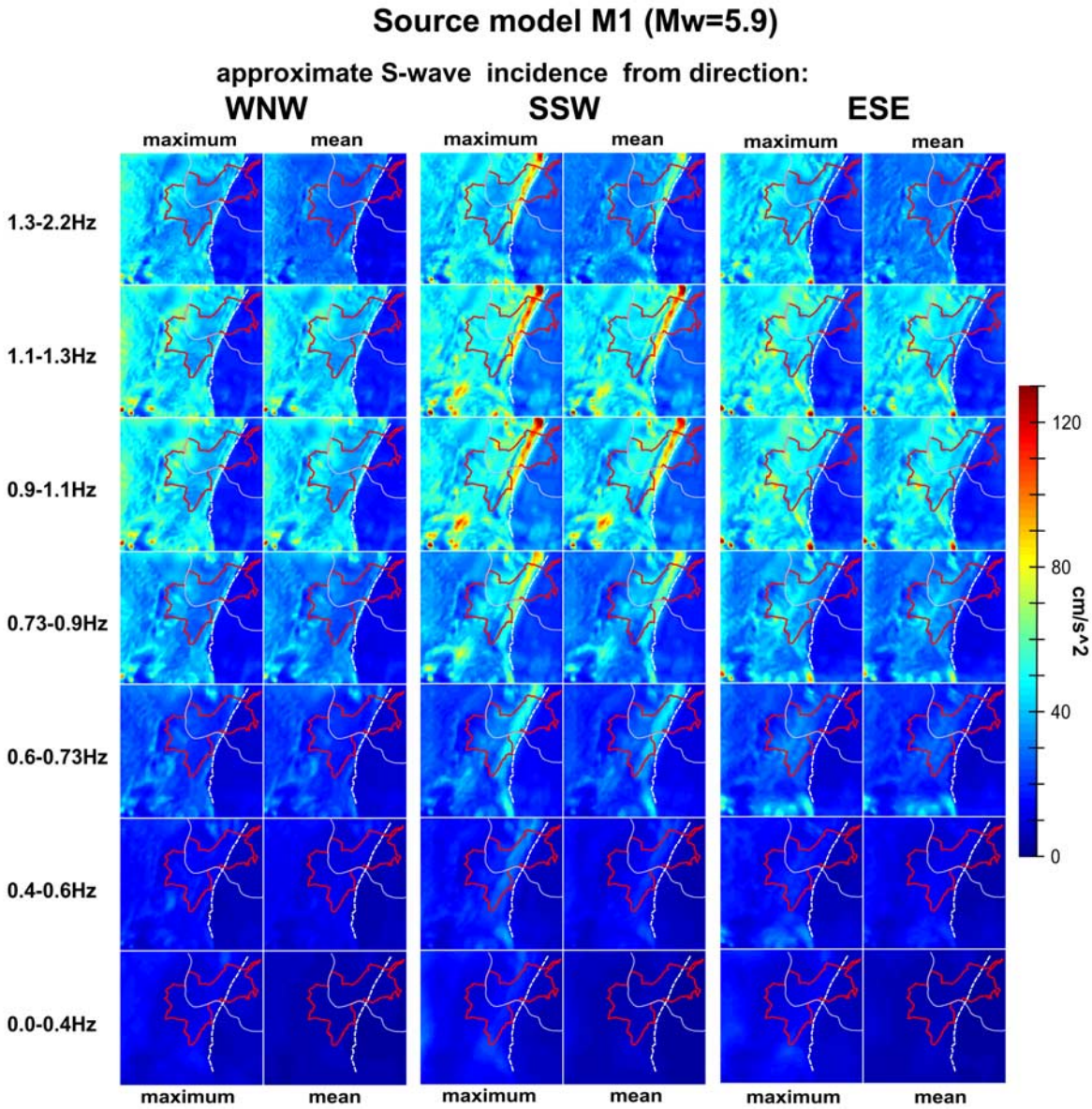

Figure 10. Pseudoacceleration response (damping 5%) for M1 finite extent source and three source positions (see the auxiliary material). WNW, SSW, and ESE denote the approximate position of the source (see Figure 2). The results are shown for a set of frequency bands. The left and right sides of each panel correspond to the maximum and mean amplitudes in the frequency band. The red line denotes Basel city limits; dashed white line the surface trace of the Rhine Graben master fault; thick gray line is the Rhine river (compare to Figure 13).

1.6 Hz in two dimensions is rather indistinct in the 3-D modeling. A single peak is present at 2 Hz for enveloped results. Data in M2 (Figure 7) are consistent with the 2-D data. Highest amplification is ~4.25.

[36] 2. Zone 2 is at (0.6–0.73) Hz, with 682 receivers: High amplifications for 0.6 and 0.9 Hz, splitting into two peaks in the envelopes. Highest amplification is ~4.125. Results from 3-D and 2-D modeling at the maximum PSA amplification agree well in averaged values. A secondary peak at about 2 Hz is indicated.

[37] 3. Zone 3 is at (0.73–0.9) Hz, with 651 receivers: The enveloped maximum amplification is slightly shifted from 0.7–1.0 Hz in the 2-D case to 0.8–1.1 Hz in the 3-D case. At ~2 Hz we can see hint of a peak. In 3-D results, the maximum amplitudes show good agreement with the 2-D results. Highest amplification is ~4.25.

[38] 4. Zone 4 is at (0.9–1.1) Hz, with 491 receivers: Shift of the maximum amplification is from 0.7–1.0 Hz in 2-D case to 1.0–1.2 Hz in 3-D case. Peak at 2 Hz is not present in the 3-D result. Highest amplification is about 3.25.

[39] 5. Zone 5 is at (1.1–1.3) Hz, with 199 receivers: The maximum amplification is shifted from 1.3 Hz to 1.5 Hz. Highest amplification is about 4.

[40] An overall feature of the 3-D versus 2-D simulations is that we typically observe higher amplification in

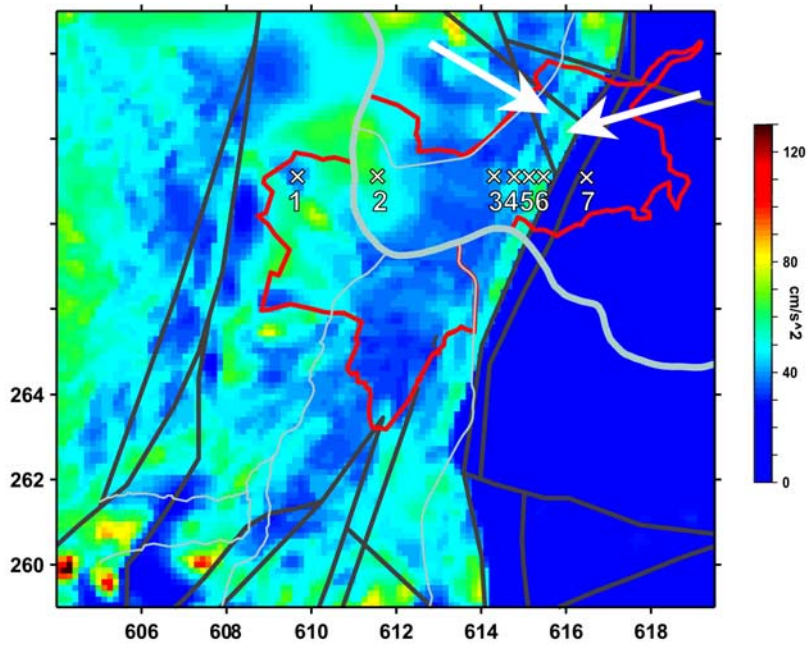

Figure 11. Maxima of PSA corresponding to frequency zone 4 (0.9–1.1 Hz) of Figure 10. The fringes mentioned in 5.2 are indicated by white arrows. Seven receivers R1–R7 are placed on the free surface. The receivers are aligned on E-W profile (269.1 km north), and the E-W positions are (609.6, 611.5, 614.4, 614.8, 615.1, 615.5, 616.5) km east for R1–R7, correspondingly.

enveloped averages for 3-D case and frequencies above (0.8–1.4) Hz. As to the enveloped amplitudes, the 3-D resulting maxima over a particular domain are very comparable in zones 3, 4, and 5. This agreement might be due to the source positions. Although *Kind* [2002] assumes the source location in the east and west of the city, our location is also to the south. Therefore it is very probable that in a large region (e.g., area 1), there will be a "better chance" for 3-D behavior expressed by a local focusing that would not appear in the 2-D case. This effect leads to slightly higher enveloped amplitudes in all regions for frequencies above ~1 Hz. The envelopes for the M1, M2 and M3 source models are very close to the results of *Kind* [2002] at zones 3, 4, and 5 (see Figure 8).

[41] The different amplitudes and shapes of the PSA curves are due to multievent analysis combined with 3-D effects, and also because the reference is not a pure 1-D model. In fact, it is a 3-D model where the interfaces copy the free surface above, and for depths larger than 1000 m it is identical with the 3-D model given by *Kind* [2002]. This three dimensionality may influence the wave field.

[42] The comparison between the 3-D and 2-D zonations (five zones within the Rhine Graben) suggests that for some applications it may be sufficient enough to apply 2-D modeling and to consider only *SH* wave propagation response while saving computer memory and time.

[43] To see the effects caused by one of the main faults (the Allschwill fault, Figure 1), we added two new zones 6 and 7, situated east and west of this fault, respectively (Figure 9). Zone 6 is defined over shallow and zone 7 over deep sediments. The principal difference compared to subdivision into zones 1–5 is that zones 6 and 7 lie on opposite sides of this buried fault. Observed PSA amplification ratios show substantial mutual differences: Zone 6 has a maximum of the envelope at about 1.3 Hz (PSA amplification of 3.6) and another at 0.95 Hz (PSA amplification of 3.8) with relatively high PSA amplifications of about 3.5 between these two frequencies. The reason is that the sediments in this area are generally very thin. In contrast, zone 7 shows a maximum PSA amplification of 3.3 at 0.6 Hz with much slower falloff in direction to lower frequencies than in the case of zone 6. A peak at 0.55 Hz, apparent in envelopes of zone 7, indicates lower positioned bottom of the upper soft sediments due to the presence of the fault.

5.2. Spectral Response (M1)

[44] In which areas, for all or some of the 3-D computations, do we observe exceptionally high values of ground motion? A comparison of the PSA for models M1 and the three different source positions is shown in Figure 10. The frequency band 0–2.2 Hz is subdivided into seven subbands to help us visualize spatial variation as a function of frequency. Bands 1–5 correspond to the five fundamental frequency zones as depicted in Figure 7 (left). The maximum (Figure 7, left) and the mean (Figure 7, right) values of PSA are expressed for each subband and source position, in order to represent the variability and typical pattern of ground motion for certain frequency bands. The maxima for the lowest frequencies are in the deep parts of the Rhine Graben for all source positions, as expected from fundamental frequency measurements. With increasing frequency they move to the northwestern part of the city, called the shoulder of Basel, where the sediments thin (see Figure 1). The maximum amplification is generally in the 0.9–1.1 and 1.1–1.3 Hz frequency bands the SSW source position (Figure 7, middle panels), when the source is located south

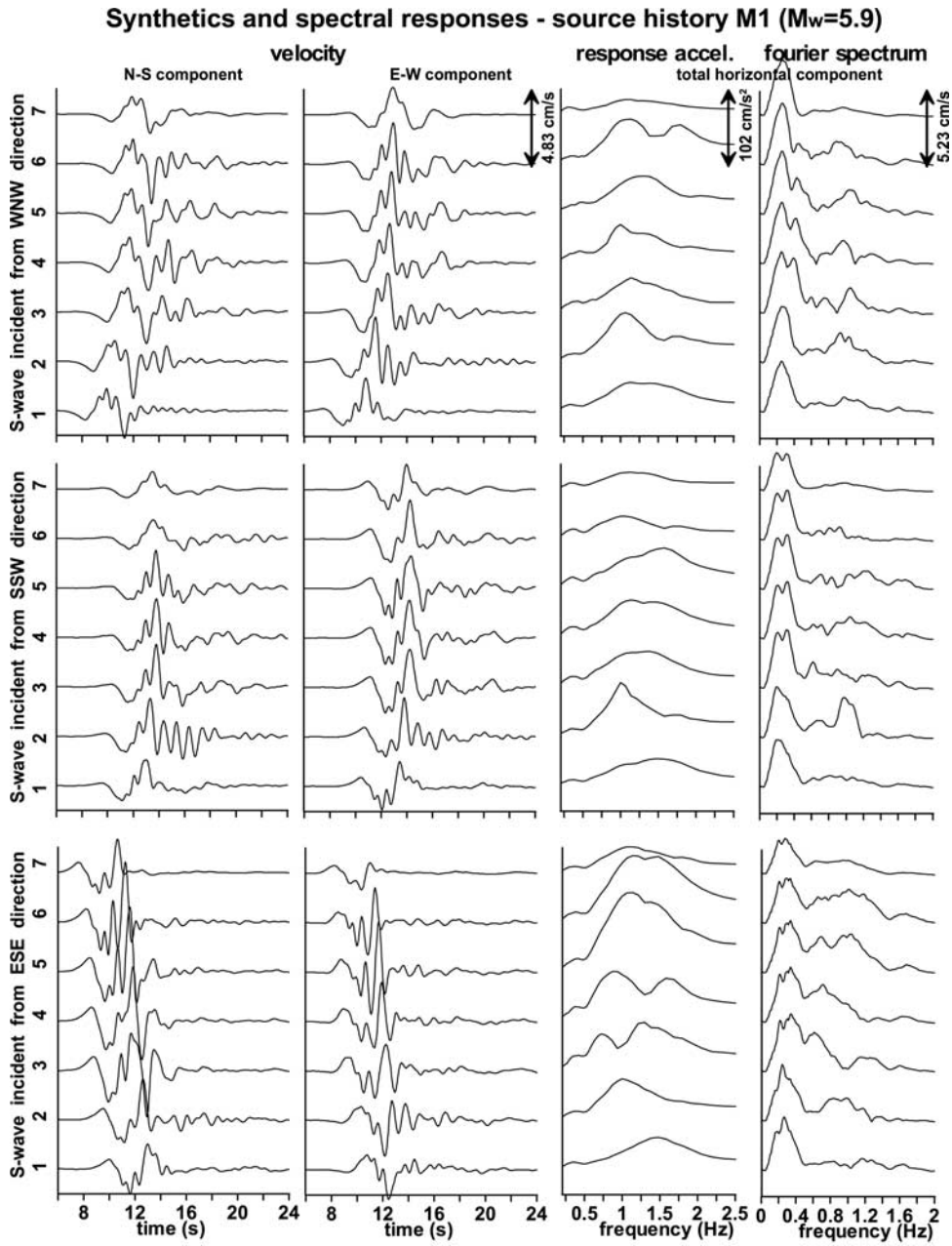

Figure 12. (left) Synthetic seismograms and their corresponding PSA for receivers R1–R7 (see Figure 11). The synthetics are computed for the M1 source placed at three positions (WNW, SSW, ESE). (right) The PSA and the Fourier spectra evaluated for total horizontal component. The arrows show the amplitudes corresponding to their denoted values.

of the city; the maximum amplitudes are approximately 130 cm s^{-2}.

[45] The WNW position of the rupture shows the maximum amplitudes (125 cm s^{-2}) in the frequency range 1.1–1.3 Hz where the maxima are found at the southwestern part on top of two hills. This strong motion on hill tops is also visible for the other source positions. Maybe it explains the effects of the 1356 event, when many castles on hill tops were severely damaged or collapsed. At a 1–2 km broad strip of higher amplitudes that stretches in the NNE-SSW direction right west of the master fault, we observe various patterns strongly depending on the position of the source. The WNW source produces two parallel fringes along the fault, roughly 1 km apart for frequencies above 0.73 Hz (Figure 10) indicated by arrows in Figure 11. They might be caused by a two-dimensional resonance or focusing of waves in the trough of St. Jakob-Thüllingen (see Figure 1). This feature is responsible for the maximum PSA amplification in zone 1 and in the frequency range 1.1–1.3 Hz. In the city area, the highest amplitudes are at the eastern part, reaching values of $\sim$70 cm s^{-2}. This area is outside the five zones proposed by *Kind* [2002] and shown in Figure 8.

[46] Regions of peak amplitudes for the SSW source location have different characteristics: The overall maxi-

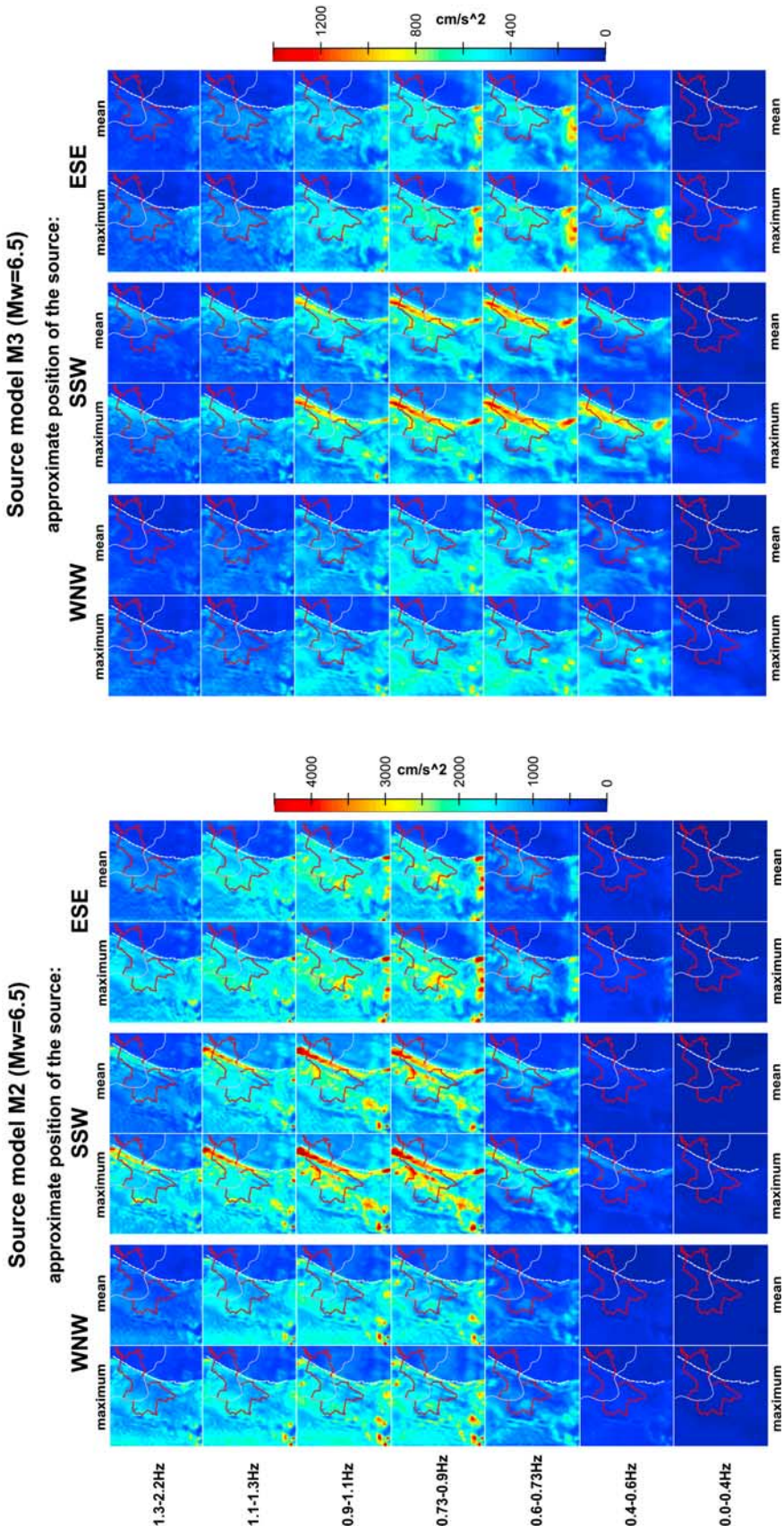

Figure 13. Pseudoacceleration response (damping 5%) for M2, and M3 finite extent sources and three source positions. WNW, SSW and ESE denote the approximate position of the source (see Figure 2). The results are shown for a set of frequency bands. The left and right sides of each panel correspond to the maximum and mean amplitudes in the frequency band. The red line denotes Basel city limits; dashed white line denotes the surface trace of the Rhine Graben master fault; thin gray line is Rhine river, and thick gray line is the Rhine river (compare to Figure 10).

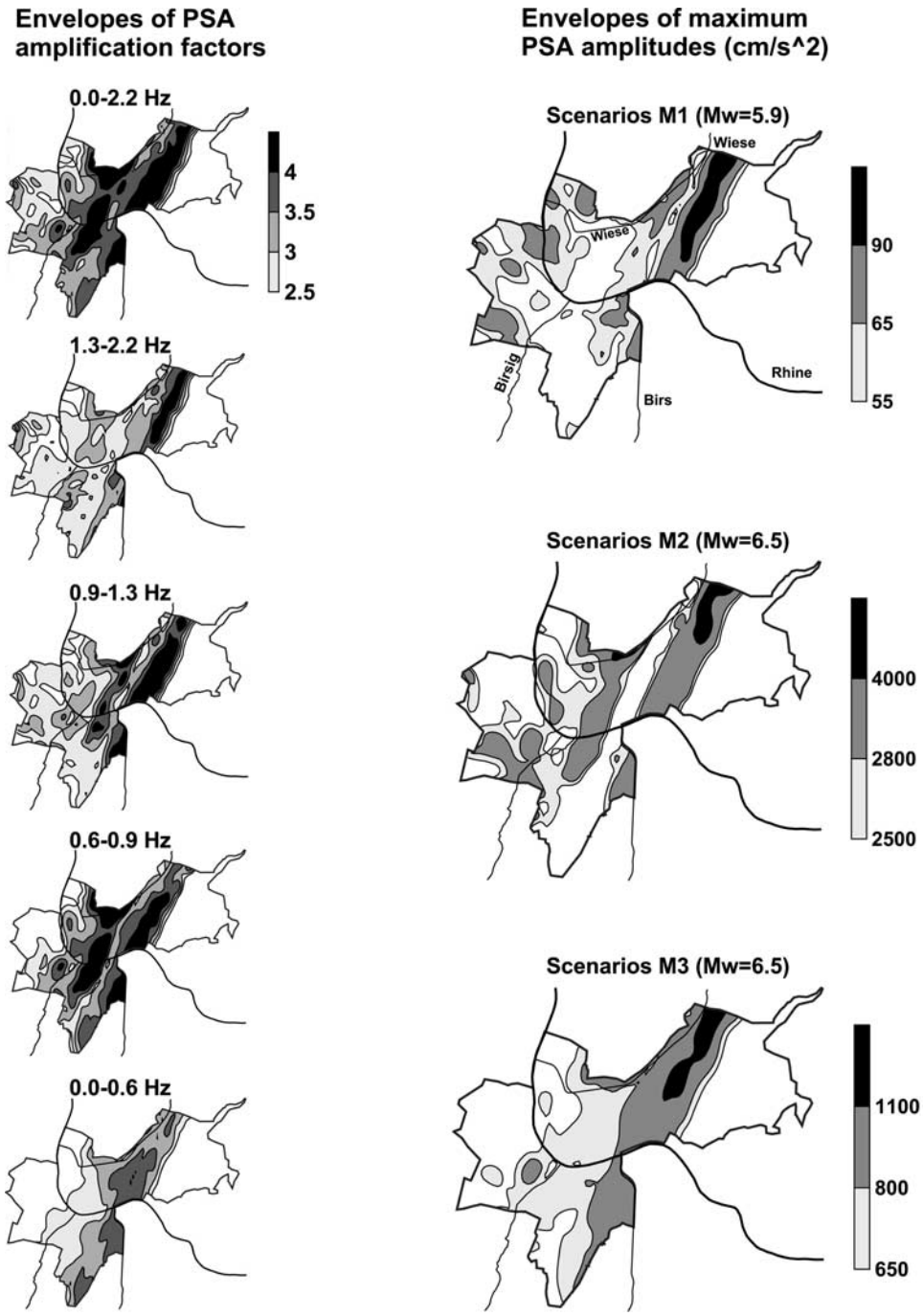

Figure 14. Potential strong motion areas of the city of Basel. (left) Zones of maximum PSA amplification dependent on the investigated frequency band, and (right) zones of maximum PSA amplitudes for specific scenarios. Black lines are the rivers Rhine (thick), Birsig, Birs, and Wiese, and gray line denotes the city limits.

mum (130 cm s^{-2}), placed right north of the city, is contained in 1-km-wide high-amplitude belt. This belt, again, extends along the western side of the master fault and is accompanied by a parallel amplitude gap and weak fringes west of it (Figure 10; 0.73–1.3 Hz). A probable reason may be that the waves are guided along the UPM layer between the dominant contrast faults (Figure 1). Other patches of high amplitudes are shown at the hills southwest of the city limits.

[47] Similarly, the high-amplification belt applies for the ESE source position, where the maximum amplitudes within the city limits are ~90 cm s^{-2}. The belt is shifted, leaving about a 1 km shadow zone west of (and along) the master fault.

[48] For all M1 cases, the strong amplification along the master fault is probably caused by a combined edge effect and guided wave phenomenon. These effects depend on the position of the rupture. (See the auxiliary material[1].)

[49] Figure 12 compares synthetic velocities (N-S, E-W components) and PSA for M1 and seven receivers R1–R7 placed on the free surface and aligned on an E-W profile as depicted in Figure 11. R1 is at the border between zones 4 and 5, R2 in zone 3, R3–R6 are covering 1-km strip west of the master fault (zone 1) and R7 is in the eastern part of the city outside the Rhinegraben.

[50] Seismograms shown in Figure 12 have lower amplitudes for receiver R7, where the PSA is strongest for the ESE source. Synthetics at R3–R6 show substantial differences between each other and indicate well the existence of the fringes mentioned above. PSA at R5 and R6 differ markedly in the WNW case, while they are very similar for the ESE case. In the latter the PSA for R5 and R6 are very similar due to a very broad high-amplification belt. PSA peak at 1 Hz for receiver R2 is narrower in SSW case than peaks in ESE or WNW cases. That indicates presence of a resonance excited due to the polarization of the *S* wave field incident approximately from SSW direction. The amplitudes of Fourier spectra for a total horizontal component are constructed as $|S(f)| = |F(S(t))|$, where F is the Fourier transformation, $S(t) = (\text{N-S}(t) + i\text{E-W}(t))/\sqrt{2}$; N-S($t$), E-W($t$) are the time histories of the respective horizontal component of velocity, and i is the complex unit. The spectra show a main peak in the interval 0.2–0.4 Hz; a significant secondary peak at about 1 Hz appears in all cases for receiver R2. Other peaks appear at frequencies 1.7 Hz for receivers R4, R5, and R6.

5.3. Spectral Response (M2, M3)

[51] M2 and M3 (M_w = 6.5) are larger earthquakes than M1. They have two prevailing rupture propagation directions, M2 "toward" and M3 "away from" the city. This difference results in a substantial difference in the duration of the incoming wave field. The frequency content is shifted toward lower frequencies for M3. Maximum PSA amplitudes are ~4500 cm s^{-2} (M2) and ~1400 cm s^{-2} (M3) (see Figure 13). At such ground motion levels, nonlinear effects play a substantial role. These effects would substantially reduce the amplitude of the ground motion and therefore our results may serve as an upper limit for presented cases. The overall high amplitudes are caused by local amplification (gravel layers) and by rather high values of the excitation wave field (~1.5 m s^{-1}) due to inverted Loma Prieta source. The main characteristics of the scenarios are the same as in the M1 case: fringes and a high-amplification belt along the master fault, the source position south of Basel (SSW case) shows the highest amplitudes, and the source position west of Basel (WNW case) causes lower amplitudes along (and west of) the master fault. Added to that, the SSW case of the M2 shows another amplification belt at the western part of zone 1. Contrary to the M2 and M3 cases, there is a "shadow" belt just west of and along the master fault in the M1 case for ESE position of the rupture. High amplitudes then (M1 case) do not appear right along the master fault but about 1 km west of it.

6. Conclusions and Prospects

[52] Our earthquake scenario modeling for the city of Basel illustrates several important properties: models with the position of the rupture at SSW show generally stronger amplification just to the west and along the master fault. This may be a potentially strong damage zone. It is probably caused by combination of edge effects and waves guided by the lower Tertiary sediments. The presence of these sediments is also the reason why the general distribution of the maxima within the city limits is more scattered in the SSW cases. The ESE and WNW sources feature fringes at higher frequencies instead of the single amplification belt. Models M1, M2, and M3 with a WNW source show smaller amplification in the eastern part of the city than corresponding models with an ESE source position. A very good fit of the measured fundamental frequencies and response spectra verifies the accuracy of the digital geological model. The frequency zoning shows a good fit to the 2-D computed data for the assigned frequency zones of the city, and amplifications were comparable. This success is due to the division of the entire area into only five zones. However, modeling allows us to highlight the areas where high PSA amplification is expected. These areas appear west of the master fault. Patches right along the fault are stretched in the NNE-SSW direction and occupy mainly the middle and northern part of the specified area. Other such regions include: the eastern coast of the Rhine river just before it leaves the city, along the Wiese river (the northernmost shown affluent of Rhine), and along the southwestern part of the city limits (approximately where the Birsig river enters). The higher PSA amplification and amplitude zones are indicated in Figure 14. The site does not feature long-period oscillations typical of closed sedimentary basins. Generally, the largest amplitudes are obtained for the following: M_w = 6.5 source with propagation "toward" the city (M2) and situated SSW of Basel.

[53] **Acknowledgments.** The manuscript benefited from helpful review comments of Associate Editor J. Townend, reviewer F. Luzón, and an anonymous reviewer. This research is part of the European project EVG1-CT-2000-00023 SAFE (Slow active faults in Europe: Assessing fundamental input for seismic risk in regions of low seismicity), BBW contract 00.0336. The computations are enabled thanks to a microaccount and help service at computing facilities of CSCS (Calcolo Scientifico Centro Svizzero), Manno, Switzerland. Code for PEXT source modeling and the source characteristics of the 1999 Athens earthquake were kindly provided by Jiri Zahradník, Charles University, Prague. This paper is contribution 1355 of the Geophysical Institute of ETH Zurich.

References

Ambraseys, N., P. Smit, R. Berardi, D. Rinaldis, F. Cotton, and C. Berge-Thierry (2000), Dissemination of European strong-motion data [CD-ROM], Eur. Counc., Environ. and Clim. Res. Programme, Brussels.

Bielak, J., K. Loukakis, Y. Hisada, and C. Yoshimura (2003), Domain reduction method for three-dimensional earthquake modeling in localized regions, part I: Theory, *Bull. Seismol. Soc. Am.*, *93*, 817–824.

Bouchon, M. (1981), A simple method to calculate Green's functions for elastic layered media, *Bull. Seismol. Soc. Am.*, *71*, 959–971.

Coutant, O. (1989), Programme de simulation numerique AXITRA, report, Lab. de Geophys. Interne et Tectonophys., Univ. Joseph Fourier, Grenoble, France.

Fäh, D., P. Suhadolc, S. Mueller, and G. F. Panza (1994), A hybrid method for the estimation of ground motion in sedimentary basins: Quantitative modeling for Mexico City, *Bull. Seismol. Soc. Am.*, *84*, 383–399.

[1]Auxiliary material is available at ftp://ftp.agu.org/apend/jb/2004JB003188.

Fäh, D., E. Rüttener, T. Noack, and P. Kruspan (1997), Microzonation of the city of Basel, *J. Seismol.*, *1*, 87–102.

Fäh, D., F. Kind, K. Lang, and D. Giardini (2001), Earthquake scenarios for the city of Basel, *Soil Dyn. Earthquake Eng.*, *21*, 405–413.

Fäh, D., et al. (2003), Earthquake catalogue of Switzerland (ECOS) and the related macroseismic database, *Eclogae Geol. Helv.*, *96*, 219–236 doi:10.1007/s00015-003-1087-0.

Graves, R. W. (1996), Simulating seismic wave propagation in 3D elastic media using staggered-grid finite differences, *Bull. Seismol. Soc. Am.*, *86*, 1091–1106.

Guatteri, M., P. M. Mai, G. C. Beroza, and J. Boatwright (2003), Strong-ground motion prediction from stochastic-dynamic source models, *Bull. Seismol. Soc. Am.*, *93*, 301–313.

Guatteri, M., P. M. Mai, and G. C. Beroza (2004), A pseudo-dynamic approximation to dynamic rupture models for strong ground motion prediction, *Bull. Seismol. Soc. Am.*, *94*, 2051–2063.

Irikura, K., and K. Kamae (1994), Estimation of strong motion in broad-frequency band based on a seismic source scaling model and an empirical Green's function technique, *Ann. Geofis.*, *37*, 1721–1743.

Irikura, K., K. Kudo, H. Okada, and T. Sasatani (Eds.) (1999), *The Effects of Surface Geology on Seismic Motion*, vol. 3, *Proceedings of ESG'98, December 1–3, 1998, Yokohama, Japan*, A. A. Balkema, Brookfield, Vt.

Kalogeras, I., and G. Stavrakakis (1999), Processing of the strong-motion data from the September 7th, 1999 Athens earthquake, report, Geodyn. Inst., Natl. Obs. of Athens, Athens, Greece.

Kind, F. (2002), Development of microzonation methods: Application to Basel, Switzerland, Ph.D. thesis 14548, ETH Zurich, Zurich, Switzerland. (available at www.seismo.ethz.ch/hazard/risk/pdf/diss_kind.pdf)

Kind, F., D. Fäh, and D. Giardini (2005), Array measurements of *S*-wave velocities from ambient vibrations, *Geophys. J. Int.*, *160*, 114–126.

Luzón, F., S. A. Gil-Zepeda, F. J. Sánchez-Sesma, and C. Ortiz-Alemán (2004), Three-dimensional simulation of ground motion in the Zafarraya Basin (southern Spain) up to 1.335 Hz under incident plane waves, *Geophys. J. Int.*, *156*, 584–594.

Mai, P. M., and G. C. Beroza (2000), Source-scaling properties from finite-fault rupture models, *Bull. Seismol. Soc. Am.*, *90*, 604–615.

Mai, P. M., and G. C. Beroza (2002), A spatial random field model to characterize complexity in earthquake slip, *J. Geophys. Res.*, *107*(B11), 2308, doi:10.1029/2001JB000588.

Mai, P. M., M. Guatteri, and G. C. Beroza (2001), A stochastic-dynamic earthquake source model for strong motion prediction: Earthquake scenarios on the Hayward-Rodgers-Creek fault system, *Eos Trans. AGU*, *82*(47), Fall Meet. Suppl., Abstract S31C-11.

Margaris, B. N., and P. M. Hatzidimitriou (2002), Source spectral scaling and stress release estimates using strong-motion records in Greece, *Bull. Seismol. Soc. Am.*, *92*, 1040–1059.

Meghraoui, M., B. Delouis, M. Ferry, D. Giardini, P. Huggenberger, I. Spottke, and M. Granet (2001), Active normal faulting in the upper Rhine graben and paleoseismic identification of the 1356 Basel earthquake, *Science*, *293*, 2070–2073.

Noack, T. (1993), Geologische Datenbank der Region Basel, *Eclogae Geol. Helv.*, *86*, 283–301.

Noack, T., P. Kruspan, D. Fäh, and E. Rüttener (1999), Mikrozonierung von Basel Stadt, *Geolog. Ber., 24*, Bundesamt für Wasser und Geol., Bern, Switzerland.

Olson, A. H., J. A. Orcutt, and G. A. Frazier (1984), The discrete wave-number finite element method of synthetic seismograms, *Geophys. J. R. Astron. Soc.*, *77*, 421–460.

Opršal, I., and J. Zahradník (2002), Three-dimensional finite difference method and hybrid modeling of earthquake ground motion, *J. Geophys. Res.*, *107*(B8), 2161, doi:10.1029/2000JB000082.

Opršal, I., J. Brokešová, D. Fäh, and D. Giardini (2002), 3D hybrid ray-FD and DWN-FD seismic modeling for simple models containing complex local structures, *Stud. Geophys. Geod.*, *46*, 711–730.

Opršal, I., J. Zahradník, A. Serpetsidaki, and G.-A. Tselenits (2004), 3D hybrid simulation of the source and site effects during the 1999 Athens earthquake, paper presented at 13th World Conference on Earthquake Engineering, Can. Assoc. for Earthquake Eng., Vancouver, B. C., Canada, 1–6 Aug.

Serpetsidaki, A. (2004), Ground motion study of the Attica earthquake of the 7th September 1999 (in Greek), Ph.D. thesis, Seismol. Lab., Geol. Dep., Patras Univ., Patras, Greece.

Somerville, P., K. Irikura, R. Graves, S. Sawada, D. Wald, N. Abrahamson, Y. Iwasaki, T. Kagawa, N. Smith, and A. Kowada (1999), Characterizing crustal earthquake slip models for the prediction of strong ground motion, *Seismol. Res. Lett.*, *70*, 59–80.

Spudich, P., and L. Xu (2003), Software for calculating earthquake ground motions from finite faults in vertically varying media, in *International Handbook of Earthquake and Engineering Seismology*, vol. 2, edited by W. H. K. Lee et al., pp. 1633–1634, Springer, New York.

Steimen, S., D. Fäh, F. Kind, C. Schmid, and D. Giardini (2003), Identifying 2D resonance in mircotremor wave fields, *Bull. Seismol. Soc. Am.*, *93*, 583–599.

Yoshimura, C., J. Bielak, Y. Hisada, and A. Fernandez (2003), Domain reduction method for three-dimensional earthquake modeling in localized regions, part II: Verification and applications, *Bull. Seismol. Soc. Am.*, *93*, 825–840.

Zahradník, J. (1995), Simple elastic finite-difference scheme, *Bull. Seismol. Soc. Am.*, *85*, 1879–1887.

Zahradník, J., and G.-A. Tselentis (2002), Modeling strong-motion accelerograms by PEXT method, application to the Athens 1999 earthquake, in *Proceedings of XXVIII General Assembly, 1–6 Sept. 2002, Genoa* [CD-ROM], Eur. Seismol. Comm., Edinburgh. (available at http://seis30.karlov.mff.cuni.cz/)

Zahradník, J., J. Jech, and P. Moczo (1990a), Absorption correction for computations of a seismic ground response, *Bull. Seismol. Soc. Am.*, *80*, 1382–1387.

Zahradník, J., J. Jech, and P. Moczo (1990b), Approximate absorption corrections for complete *SH* seismograms, *Stud. Geophys. Geod.*, *34*, 185–196.

Zechner, E., F. Kind, D. Fäh, and P. Huggenberger (2001), 3-D geological model of the southern Rhinegraben compiled on existing geological data and geophysical reference modeling, paper presented at the 2nd EUCOR-URGENT Workshop, Eur. Sci. Found., Strasbourg, France, 7–11 Oct.

D. Fäh, D. Giardini, P. M. Mai, and I. Opršal, Swiss Seismological Service, Swiss Federal Institute of Technology, ETH-Hoenggerberg, CH-8093 Zurich, Switzerland. (ivo@sed.ethz.ch)